MICRO- OR NANO-MECHANICS

A review of adhesion mechanisms of mushroom-shaped microstructured adhesives

Giuseppe Carbone · Elena Pierro

Abstract Very recently, both experimental and theoretical investigations have shown that micro-structured surfaces covered with mushroom shaped micropillars present strongly enhanced adhesive properties if compared to standard flat surfaces made of the same material. However, different geometries lead to different adhesive performance, and finding the optimal solution has become of utmost importance. In this review we summarize the main detachment mechanisms of flat-topped and mushroom-topped soft micro pillars and show how the geometry of the pillars should be designed in order to obtain the best adhesive performances. We also discuss the effect of air entrapment at the interface between the pillar and the substrate and investigate the influence of the non uniform pillar height and thermal fluctuations on pull-off force.

Keywords Biomimetics · Microstructures · Adhesives · Contact mechanics · Crack propagation

G. Carbone (✉)
TriboLAB, Dipartimento di Ingegneria Meccanica
e Gestionale, Politecnico di Bari, V.le Japigia 182,
70126 Bari, Italy
e-mail: carbone@poliba.it

E. Pierro
Scuola di Ingegneria, Università degli Studi della
Basilicata, 85100 Potenza, Italy

1 Introduction

Biomimetics has always played a crucial role in suggesting, conceiving and developing breakthrough solutions in mechanical, material and civil engineering, e.g.: (i) Velcro has been inspired by the hooks of burs, (ii) lumberjack blades have been inspired by wood-burrowing beetle, (iii) cat's eye reflectors have been inspired by the cats' system of reflecting cells, known as *tapetum lucidum*, (iv) 'morphing aircraft wings', that change shape according to the speed, have been inspired by different bird species, (v) some paints and window surfaces have been engineered to be self-cleaning as in the case of lotus leaf, (vi) the cooling system of the Eastgate Centre building, in Harare, has been inspired by a termite mound [1]. In the last years, bio-inspired adhesive structures have drawn great attention from the research community [2–13], due to their extremely high adhesive performance. In nature, many biological attachment systems (e.g. Gecko foot pad [14]) are made of hairs which are constituted mainly of a relatively stiff material, the β-keratin (elastic modulus $E \approx 1$ GPa). In this case, as suggested by some experimental findings and theoretical investigations [15–26], the compliant fibrillar hierarchical geometry of such structures provides them with amazing adhesive properties. However, examples exist in Nature, e.g. the attachment pad of the males of some beetle species from the family Chrysomelidae, which do not present a hierarchical geometry as Gecko does, but are simply surfaces covered with mushroom-

shaped microstructures [27–29]. In such cases [7], the shape of the terminal plate is crucial for the achievement of high adhesive strength values of the bio-inspired artificial surfaces [30]. In particular, experimental observations [7] have shown that mushroom shaped microstructures [Fig. 1(a, b, c)] strongly outperform, in terms of pull-off force, surfaces covered with miniaturized cylindrical pillar made of the same material [polyvinylsiloxane (PVS), Young's modulus $E = 3$ MPa].

This property has been very recently exploited to develop bio-inspired band-aids [31, 32]. However, different mushroom-pillar geometries have led to different experimental results [21, 33] and to some differences if compared to theoretical predictions [30]. In this review we summarize the main findings, that explain the origin of the superior performance of mushroom shaped micropillars. The paper is organized as follows. In Sect. 2 we present the mechanisms which govern the detachment of cylindrical micro-pillars. In Sect. 3 we show that the presence of the plate in mushroom shaped pillar inhibits one of the detaching modes, leading to a strong increase of the pull-off force. In Sect. 4 we show how the geometry of the mushroom-shaped pillar may be optimized to increase the adhesive performance. In Sect. 5 we discuss the effect of entrapment of air at the interface on the pull-off force. In Sect. 6 we present a different detaching mechanism which may occur on perfectly clean surfaces as a consequence of stress aided thermally activated defect nucleation. In Sect. 7 we show how the non uniform micro-pillar height distribution affects the adhesive performance of the system. In Sect. 8 we provide concluding remarks and outline future developments.

2 The cylindrical micropillar

Let us first consider in detail the case of a cylindrical micropillar in contact with a perfectly flat substrate [Fig. 1(d)]. Let us assume the pillar is loaded with a tractive force P. In principle the detachment of the pillar from the substrate may be governed by three different mechanisms depending on the work of adhesion (also referred to as the Duprè energy of adhesion) $\Delta\gamma = \gamma_1 + \gamma_2 - \gamma_{12}$ (where γ_1 is the surface energy of solid 1, γ_2 is the surface energy of solid 2 and γ_{12} is the surface interaction energy
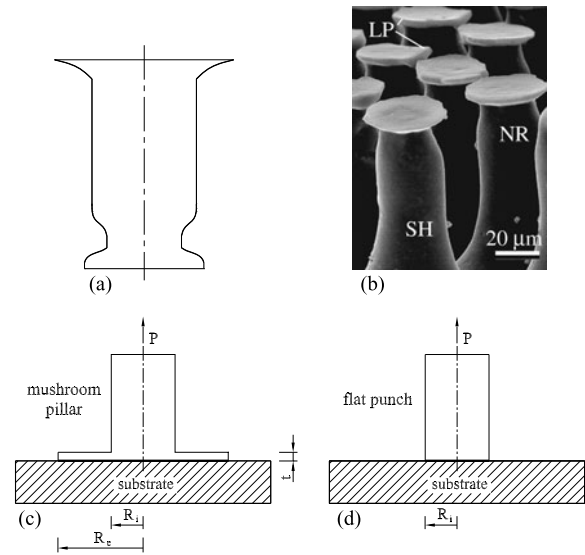

Fig. 1 A schematic drawing of a single mushroom shaped pillar, (**a**); a SEM image of microfabricated PVS mushroom shaped pillars (courtesy of prof. Gorb [33]), (**b**); the mushroom shaped pillar, (**c**); and the cylindrical pillar (**d**) in contact with a rigid substrate. The terminal plate in the mushroom shape (**c**) is the origin of the enhanced adhesive performance

when the two surfaces are in direct contact), on the geometry of the pillar, and on Young's modulus E of the material: (I) crack propagation from the pillar edge [Fig. 2(a)], (II) propagation of interfacial defects from the inner side [Fig. 2(b)], (III) decohesion due to the achievement of theoretical contact strength $\sigma_{III} = \Delta\gamma/\rho$ where $\rho \approx 1$–10 nm is the typical range of van der Waals forces [Fig. 2(c)]. Dimensional arguments for mode I debonding of micro-pillars of radius R in contact with the substrate, allow to assert that crack propagation from the edge initiates when the average tractive stress at the interface exceeds the value

$$\sigma_I = CE^* \left(\frac{8}{\pi} \frac{\delta}{R} \right)^\lambda \tag{1}$$

where $E^* = E/(1 - \mu^2)$, $\mu = 0.5$ is Poisson's ratio, $\delta = \Delta\gamma/E^*$ is the adhesion length, λ is the order of stress singularity [34] at the edge of the pillar and depends on the corner angle θ and on the boundary conditions at the interface (no-slip, partial-slip, no friction). In the case of cylindrical pillars $\theta = \pi/2$ and assuming sticking friction at the interface one has $\lambda = 0.4$ for incompressible materials [34]. The dimensionless quantity C is a constant factor which mainly depends on the geometry and on the frictional state at the interface. In the case of a cylindrical pillar indenting an
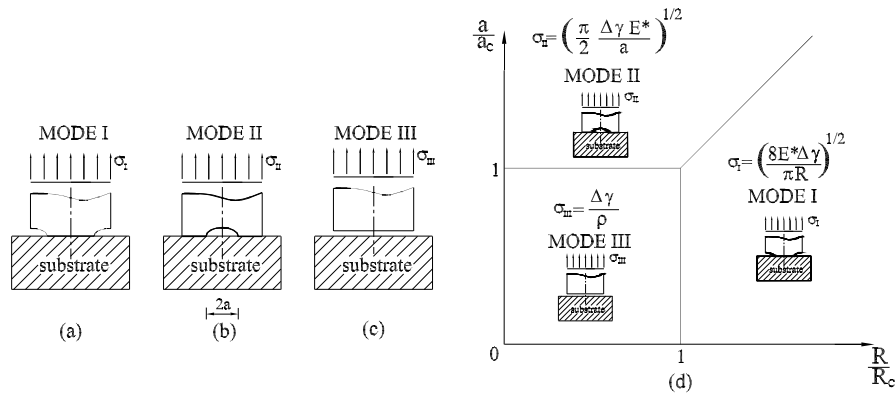
Fig. 2 Debonding of a cylindrical pillar may occur because of crack propagation from the pillar edge (**a**), nucleation and propagation of interfacial defects (**b**), decohesion due to the achievement of the theoretical contact strength (**c**). Map of debonding mechanisms of a cylindrical pillar (**d**). The quantities $a_C = \frac{1}{2}\pi E^* \rho^2 / \Delta\gamma$ and $R_C = (8/\pi) E^* \rho^2 / \Delta\gamma$ are respectively a reference defect size and a reference pillar radius

elastic half-space ($\theta = \pi$) and no friction at the interface, one has $\lambda = 1/2$ and $C = 1$. Equation (1) can be easily derived by observing that at the edge of the contact the stress $\sigma_{ij} \approx r^{-\lambda}$ [34] where r is the distance from the edge. Therefore the critical stress $\sigma_I \approx R^{-\lambda}$. However σ_I must also depends on E^* and $\Delta\gamma$, hence invoking Buckingham's theorem [35, 36] one can write $\sigma_I / E^* \approx (\delta/R)^\lambda$, from which Eq. (1) follows. The strength of stress singularity at the edge is identified by the stress intensity factor K defined through the relation $\sigma_{ij} = K(2\pi r)^{-\lambda} f_{ij}(\varphi)$, where $f_{ij}(\varphi)$ is a non-dimensional function of material parameters, corner angle, λ, and polar co-ordinate φ. Dimensional arguments allow also to assert that $K \approx \sigma_0 (\pi R)^\lambda$ where σ_0 is the far field applied stress. Therefore mode I detachment will occur when K reaches the critical intensity

$$K_c = \frac{1}{2}\alpha \sigma_I (\pi R)^\lambda = \frac{1}{2}\alpha C E^* (8\delta)^\lambda$$
$$= \frac{1}{2}\alpha C E^{*1-\lambda}(8\Delta\gamma)^\lambda \tag{2}$$

where α is a constant of order unity. Equation (2) allows us to define an effective energy release rate G as

$$G = \frac{2^{1/\lambda}}{4\alpha^{1/\lambda} C^{1/\lambda}} \frac{K^{1/\lambda}}{2E^{*1/\lambda-1}} \tag{3}$$

so that the critical condition for crack propagation from the edge of the pillar can be written in the usual Griffith form $G = \Delta\gamma$. Of course in the case of a rigid cylindrical pillar in frictionless adhesive contact with

an elastic half-space ($\lambda = 1/2$) one obtains the usual definition $G = K_I^2 / (2E^*)$, with $\alpha = C = 1$.

Note that Eq. (1) is confirmed by more accurate calculations [37], which have been carried out within the framework of the Dugdale-Barenblatt cohesive zone. These calculations show that, for elastic cylindrical pillars in sticking contact with a flat rigid substrate, the critical mode I debonding stress is

$$\sigma_I \approx B \left(\frac{\sigma_{th}}{E^*}\right)^{1-2\lambda} E^* \left(\frac{\delta}{R}\right)^\lambda \tag{4}$$

which is the same as Eq. (1) except for a factor of order unity $(\sigma_{th}/E^*)^{1-2\lambda}$, that is independent of the pillar geometry, where σ_{th} is the interfacial theoretical strength.

Now let us consider that, since the exponent λ depends on the real geometry and on the real boundary conditions (e.g. no-slip, partial slip, no friction) at the interface, its value is not easy to estimate. Therefore, in what follows we will assume $\lambda \approx 0.5$. This assumptions limit nowise the general validity of our treatment and main conclusions. So we assume that the mode I pull-off stress, needed to separate an elastic cylindrical pillar in adhesive contact with a rigid substrate, is

$$\sigma_I \approx E^* \left(\frac{8}{\pi} \frac{\delta}{R}\right)^{1/2} = \left(\frac{8 E^* \Delta\gamma}{\pi R}\right)^{1/2} \tag{5}$$

As already mentioned, there is also a second debonding mechanism, i.e. the growth of interfacial cracks [Fig. 2(b)], which may occur because defects are often already present at the interface. In this case
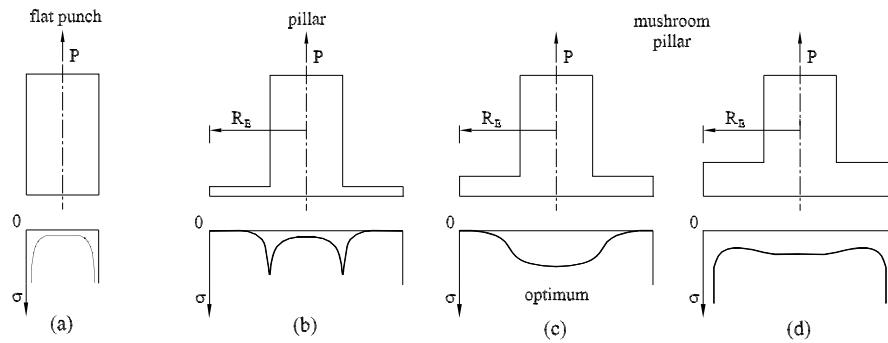
Fig. 3 Stress distribution in case of a cylindrical pillar (**a**) and for a mushroom shaped pillar, for three different thickness of the plate, thin (**b**), medium (**c**) and thick (**d**). The presence of the plate eliminates the stress singularity of the cylindrical pillar at $r \approx R$. Stress peak in the mushroom pillar at $r \approx R$ will gradually vanish as the plate thickness t is increased up to its optimal value (**c**)

the change of adhesion energy $\Delta U_{ad} = \pi a^2 \Delta \gamma$ and elastic energy $\Delta U_{el} \approx -(4\sigma^2 a^3)/(3E^*)$. To calculate the critical pull-off stress σ_{II}, consider that the change of total energy needed to generate a defect of radius a is

$$\Delta U_{tot} \approx -\frac{4}{3} \frac{\sigma^2 a^3}{E^*} + \pi a^2 \Delta \gamma \qquad (6)$$

Enforcing the condition $\partial(\Delta U_{tot})/\partial a = 0$ one can calculate for any given defect size a the critical stress σ_{II}:

$$\sigma_{II} \approx \left(\frac{\pi}{2} \frac{\Delta \gamma E^*}{a} \right)^{1/2} \qquad (7)$$

Among the three different failure mechanisms (mode I, mode II and mode III) only the one corresponding to the minimum value of the critical stresses σ_I, σ_{II} and $\sigma_{III} = \Delta \gamma / \rho$ could actually take place. A map of the debonding mechanisms can be proposed, as shown in Fig. 2(d), where the quantities $a_C = \frac{1}{2}\pi E^* \rho^2 / \Delta \gamma$ and $R_C = (8/\pi)E^* \rho^2 / \Delta \gamma$ are respectively a reference defect size, and a reference pillar radius. Let us observe that for soft cylindrical micropillars (e.g. PVS pillar [28]) assuming $\Delta \gamma \approx 16$ mJ/m^2, $\mu = 0.5$, $E = 3$ MPa, and recalling that the range of van der Waals forces is about $\rho \approx 1$ nm one obtains $a_C = 0.39$ nm and $R_c = 0.63$ nm, so that mode III debonding cannot occur in real cases where the pillar radius is of order several micrometers. Figure 2(d) also shows that cylindrical micropillars will detach by following the mode II mechanism only in the very seldom case of very large defects or impurities at the interface. In fact only when $a/a_C > R/R_C$, i.e. only if $a/R > a_C/R_C = \pi^2/16 \approx 0.62$, the stress σ_{II} is smaller than σ_I. Hence, cylindrical soft micropillars must necessarily detach by following mode I debonding. As-

suming as in [28] that the pillar has a diameter $2R \approx 15$ mm one obtains a pull-off stress $\sigma_I \approx 4.6$ kPa, and consequently a pull-off force $F_{out} = 0.8$ N in perfect agreement with experimental findings [28].

3 The mushroom shaped pillar

Some studies [7, 28] have shown that if a very compliant annular plate is added to the base of the cylindrical pillar the pull-off stress is unexpectedly strongly increased. This suggests that a different debonding mechanism should occur. Let us first observe that, the presence of the plate, if optimally designed (see also Sect. 4), may eliminate the stress singularity at $r \approx R$ [Fig. 3(a)]. However, for too thin plates a large stress peak will still be present at the interface [see Fig. 3(b)], which may facilitate the formation and propagation of cracks from the edge $r \approx R$ of the central pillar. The stress peak at $r \approx R$ will gradually vanish if the plate thickness t is increased up to an optimal value [see Fig. 3(c)], at which the stress distribution becomes almost uniform below the pillar and smoothly decreases until it vanishes at the plate perimeter $r = R_e$ [38]. In this case the uniform stress acts on a region of radius $R_\sigma \approx 1.1R$ [38]. If the thickness of the plate is increased further [see Fig. 3(d)] then the stress singularity may appear again at $r = R_e$ and the mushroom pillar will behave as a bigger and less performing cylindrical pillar. To confirm this behavior, we have carried out a Finite Element Analysis of the optimized mushroom shaped pillar, using the commercial code ANSYS. The results are shown in Fig. 4, in terms of dimensionless interfacial normal stress distribution underneath the plate $\tilde{\sigma} = \sigma / E^*$, plotted against the ratio
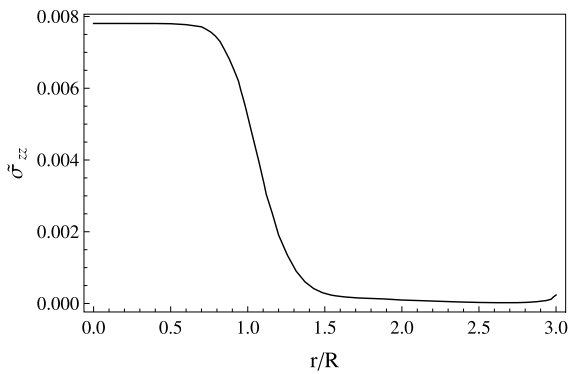
Fig. 4 The dimensionless normal stress distribution $\tilde{\sigma}_{zz}$ as a function of the ratio r/R, for an optimal mushroom shaped pillar
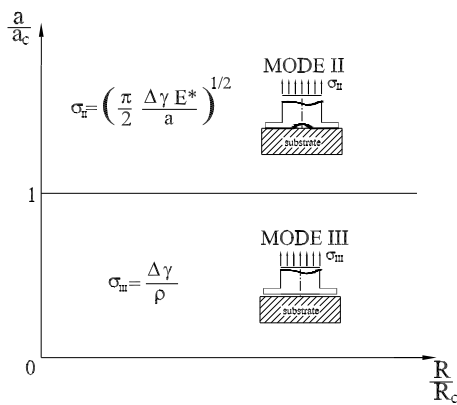

Fig. 5 Map of debonding mechanisms for an optimally designed mushroom shaped pillar. Detachments in this case must be governed by mode II or mode III debonding, depending on which one of them is energetically more favorable
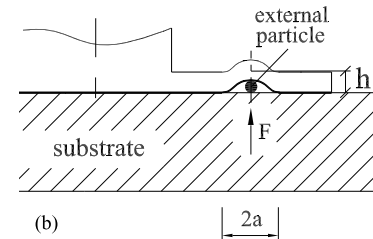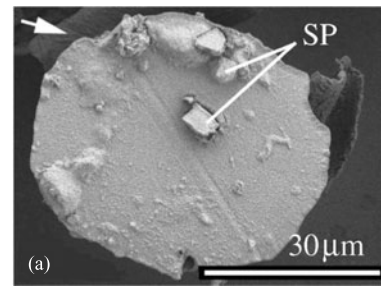

Fig. 6 Small dirt particles of about 3–5 μm in size contaminate the interface between the mushroom-shaped pillar and the substrate [33], (**a**). The presence of impurities at the interface determines a decrement of plate-substrate contact area, but, as our calculations show, does not compromise the plate stability, i.e. cannot cause defect propagation (**b**)

between the distance from the pillar center r and the internal radius R. As expected, the stress singularity at the edge of the plate is almost completely disappeared, even more the interfacial normal stress almost completely vanishes as the external contact perimeter is approached. Hence, the main role of the plate is to prevent mode I debonding from happening, thanks to the suppression of the stress singularity at the pillar edge. Therefore, in the case of optimally designed mushroom shaped micro-pillars, the most critical conditions are actually established under the central pillar at $r < R$, and detachment must follow mode II or mode III mechanisms, depending on which one of them is energetically more favorable. The debonding map is then modified as shown in Fig. 5, from which it follows that in the specific case of PVS samples under investigation ($\Delta\gamma \approx 16$ mJ/m², $E^* = 4$ MPa,

$a_C = 0.39$ nm), mode II should be the real debonding mechanism as indeed confirmed experimentally in [21]. This actually means that since mode II debonding is independent of the pillar size but depends on the defect size [see Eq. (7)], the pull-off force should be exactly the same both for thin and wide pillars, provided that the defect size is also the same in the two cases. This is indeed in perfect agreement with the experimental results presented in Refs. [28, 39]. A last consideration about the defect shape must be done. Some experimental observations have shown that defects at the interface may assume the shape of simply connected closed regions with a size much smaller than the radius R of the pillar (see Fig. 6).

Therefore, let us assume that a circular particle is found under the plate [see Fig. 6], it produces a circular defect of radius a and height h. Let us analyse the stability of the defect. This time the propagation of the defect will occur at constant height h since the size of the external particle does not change during propagation, hence the only contribution to the change of total energy will come from the change of elastic and adhesion energies. To calculate the change of elastic energy, consider that the external particle exerts on the plate a detaching force F given by

$F = 16\pi Dh/a^2$ [40, 41], where $D = E^* t^3/12$. This gives $\Delta U_{el} = \frac{1}{2} Fh$, whereas the adhesion energy is $\Delta U_{ad} = \pi a^2 \Delta\gamma$. Thus, the change of total energy is

$$\Delta U_{tot} = 8\pi D \left(\frac{h}{a}\right)^2 + \Delta\gamma \pi a^2 \tag{8}$$

As before, enforcing the condition $\partial \Delta U_{tot}/\partial a = 0$ the size of the detached area at equilibrium can be calculated as

$$a_{eq} = \left(\frac{8Dh^2}{\Delta\gamma}\right)^{1/4} \tag{9}$$

and the corresponding detaching force at equilibrium becomes $F_{eq} = 4\pi\sqrt{2D\Delta\gamma}$, which remarkably does not depend on the size of the defect, i.e. external impurities underneath the plate, will always exert the same detaching force independent of their size. Observing that $\partial^2 \Delta U_{tot}/\partial a^2$ is always positive it follows that the presence of the plate stabilizes defects at the plate-substrate interface, i.e. defects under the plate cannot propagate but stay there. We also observe that this result is in agreement with Glassmaker's work [42], who showed that the presence of a terminal film connecting the ends of the pillars reduces the amount of energy available to propagate the interfacial defects.

4 Shape optimization

Let us consider the pillar shape [33] shown in Figs. 1(a)–(b). FEM calculations have been carried out for the simplified geometry represented in Fig. 7(a). The grid [Fig. 7(b)] has been specifically generated in order to have higher elements density both at the inner radius R_i of the pillar (where interfacial stress peaks may occur) and at the outer perimeter of the pillar (where stress square-root singularities appear for non optimized geometries).

The pillar is considered to fully adhere to the flat rigid substrate, and sticking friction, observed in some experiments [21], is taken into account by properly constraining all the nodes of the adhering surface. An external normal load $P = \pi R_i^2 \sigma_0$ is, then, applied to the free end of the pillar, and the interfacial normal σ_{zz} and shear σ_{zr} stresses have been determined by means of FEM calculations. Both stress distributions show a singular behavior close to the external perimeter of the contact. The strength of such singularities is quantified by the corresponding stress intensity factors [43] K^I
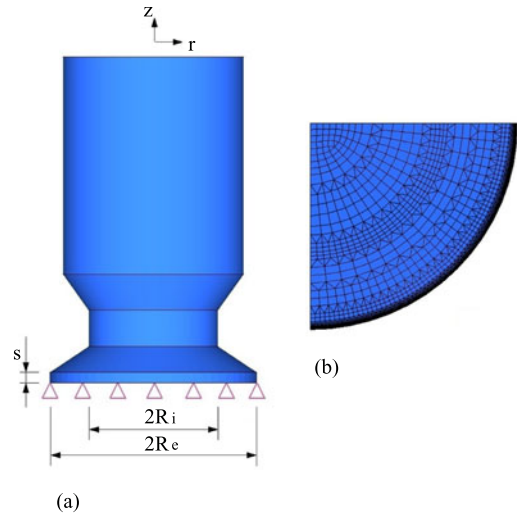

Fig. 7 A CAD model of the mushroom shaped pillar shown in Fig. 1, (**a**); and the FEM grid, (**b**)

and K^{II}. The pull-off stress is calculated by enforcing the generalized Griffith condition [43] $G = \Delta\gamma$, i.e. by requiring that G is equal to the work of adhesion $\Delta\gamma$. The stress intensity factors K^I and K^{II} can be calculated by recalling that they are proportional to the externally applied stress σ_0 and depend, given the material properties, only on the shape of the pillar [44]. Therefore, once fixed the external applied stress σ_0, a single Finite Element analysis is sufficient [44] to calculate the reduced normal and tangential stress distributions (σ_{zz}/σ_0, σ_{zr}/σ_0) at the interface and the stress intensity factors. The FE analysis has been carried out with the aid of the commercial software ANSYS [45].

As a first example, we have carried out calculation for the micropillar shown in Fig. 1(b) whose geometry has been taken from Ref. [33]. In particular the external diameter of the thin plate is $D_e = 2R_e \approx 40$ μm, the internal diameter is $D_i = 2R_i \approx 25$ μm and the thickness s of the plate is $s = 2$ μm. Calculations have shown [44] that this type of geometry is suboptimal. Indeed, the reduced normal and shear interfacial stress distributions σ_{zz}/σ_0 and σ_{zr}/σ_0, as functions of the ratio r/R_i, present an unwanted singular behavior at the external edge of the thin plate. The critical stress σ_I needed to activate mode I debonding mechanism [30] is, then, determined by enforcing the condition for crack propagation which yields $\sigma_I = CE^*[8\delta/(\pi R_i)]^\lambda$, i.e.

$$\sigma_I = \frac{1}{\tilde{K}_{eq}} E^* \left(\frac{\Delta\gamma}{\pi R_i E^*}\right)^\lambda \tag{10}$$

where $(\tilde{K}_{eq}) \approx 0.2$ is a shape factor related to the pillar geometry. Recalling that $E = 3$ MPa, $\nu = 0.5$ and $\Delta\gamma \approx 16$ mJ/m^2, and assuming $\lambda = 0.5$, the calculated critical stress is $(\sigma_I)_{FP} \approx 0.33$ MPa. We may compare these results with the measurements reported on the same microstructures [see Fig. 1(b)] by Gorb et al. [33], where a surface with diameter $d = 2.9$ mm is covered with the mushroom-shaped pillars and presents a coverage factor $\alpha = 40$ % [Fig. 1(b)]. They measured on clean surfaces a pull-off force $F_{out} \approx 350$ mN, whereas our estimated pull-off force is $F_{out} = \alpha(d^2/4R_e^2)\pi\sigma_I R_i^2 \approx 340$ mN in very good agreement with the experimental value. Of course the presence of impurities or defects at the interface may change the scenario and, in particular, may switch the debonding mechanism from mode I to mode II [30] and determine a reduction of the critical debonding stress.

The above results [see Eq. (10)] show that the critical stress for mode I debonding rapidly increases as the shape factor $\tilde{K}_{eq}$ decreases. In principle σ_I should diverge when the shape factor $\tilde{K}_{eq}$ goes to zero, i.e. when the stress singularity at the pillar edge vanishes. In this case, for soft materials [30], the mode II mechanism should become the dominant one. Noticing that, on smooth and clean surfaces, the mode II debonding mechanism is activated by stress aided thermal fluctuations (see Sect. 7 and Ref. [30]), this should lead to very high adhesive forces. However the presence of stress peaks at the interface weakens the adhesion of the pillar to the substrate and should be avoided. Therefore, an optimally designed mushroom pillar should prevent the formation of stress intensification at the interface. This can be achieved, by properly engineering the geometry of the terminal plate and, in particular, by choosing the dimensionless quantities s/R_i and R_e/R_i to guarantee an almost uniform stress distribution in the central part of the pillar $0 < r < R_i$ and a vanishing stress at the edge of the contact.

The FE analysis hereafter presented, has been carried out to investigate the influence of the two parameters R_e/R_i and s/R_i on the stress distribution under the plate.

Figure 8 shows the reduced normal stress distribution σ_{zz}/σ_0 at the interface between the mushroom shaped pillar and the rigid substrate, as a function of r/R_i, for three different values of R_e/R_i, i.e. $R_e/R_i = 2$ (a), $R_e/R_i = 3$ (b) and $R_e/R_i = 4$ (c). Results confirm what has been qualitatively discussed in Sect. 3.

Indeed calculations show that, thick plates present a stress singularity at the edge of the contact. On the other hand, for very thin plates a stress peak appears at $r = R_i$. The physical reason behind this is very simple. When the thickness of the plate is very thin, the presence of the plate itself negligibly modify the stress distribution which would be observed if the plate were completely absent. But, flat cylindrical pillars present a stress singularity at $r = R_i$.

Thus, thin plates will be only able to slightly smoothen the stress singularity, without making the peak disappear. On the other hand, very thick plates behave as larger cylindrical pillars of radius R_e and the stress singularity will then appear at $r = R_e$. The plate thickness is therefore the very crucial quantity that must be controlled to optimize the adhesive performance of the system. However, for $R_e/R_i = 2$ [Fig. 8(a)] it is not very easy to find the optimal value of s/R_i that guarantees zero stress at $r = R_e$ and avoids the stress peak at $r = R_i$, a good value is $s/R_i = 0.2$. For larger values of R_e/R_i [Fig. 8(b)–(c)] this optimal choice can be identified with $s/R_i \approx 0.3$. In conclusion the optimized geometry should be characterized by $s/R_i \approx 0.2$–0.3 and values of $R_e/R_i \geq 2$ and preferably close to 3. Values of R_e/R_i much larger than 3 should be avoided since they might reduce the coverage factor of the surface and worsen the performance of the whole adhesive.

Recalling that for a cylindrical micropillar of radius R_i the mode I debonding stress is $(\sigma_I)_{FP} = [1/(\tilde{K}_{eq})_{FP}]E^*[\Delta\gamma/(\pi E^* R_i)]^\lambda$, we can easily calculate for the case of a mushroom shaped pillar with internal radius R_i the stress enhancement factor

$$\frac{\sigma_I}{(\sigma_I)_{FP}} = \frac{(\tilde{K}_{eq})_{FP}}{\tilde{K}_{eq}} \qquad (11)$$

which provides a measure of how much the presence of the terminal plate is beneficial in enhancing the adhesive performance. Figure 9 shows, under the assumption $\lambda \approx 0.5$, the debonding maps for different type of micropillars: (i) cylindrical pillar, (ii) the non-optimized mushroom shaped pillar, and (iii) the optimized mushroom shaped pillar. We recall that the mode III debonding mechanism shown in Fig. 9 is due to the achievement of the theoretical contact strength $\sigma_{III} = \Delta\gamma/\rho$ where $\rho \approx 1$ nm is the typical range of van der Waals forces (for more details see Ref. [30]). In Fig. 9, the quantities $a_C = \frac{1}{2}\pi E^* \rho^2/\Delta\gamma$ and $R_C = E^*\rho^2/[\pi\Delta\gamma(\tilde{K}_{eq})_{FP}^2]$ are respectively a reference defect size, and a reference pillar radius. Assuming, as
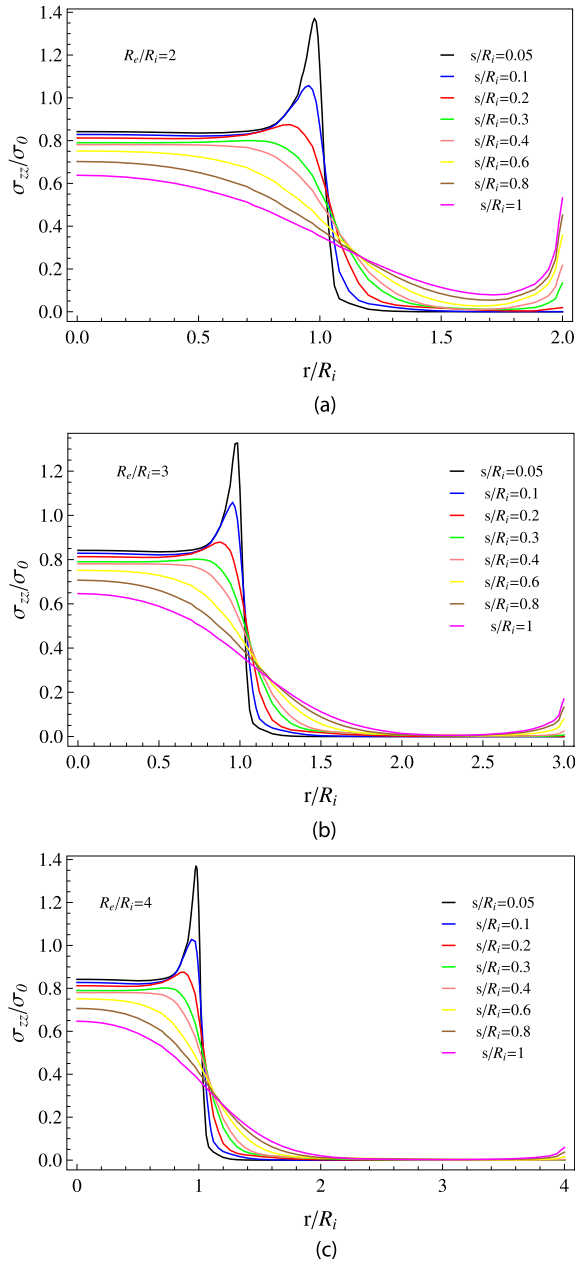
Fig. 8 The reduced normal stress distribution σ_{zz}/σ_0 as a function of r/R_i, for $R_e/R_i = 2$, (**a**); $R_e/R_i = 3$, (**b**); and $R_e/R_i = 4$, (**c**). For $R_e/R_i = 2$ (or smaller) and $0.2 < s/R_i < 1$ the stress increases at the external perimeter of the plate. For thinner plates ($s/R_i < 0.2$), on the contrary, a stress peak appears at the internal radius R_i. At larger values of R_e/R_i it is possible to find optimal configurations with $s/R_i \approx 0.2$–0.3. In this case the singularity at the $r = R_e$ almost disappears as well as the stress peak at $r = R_i$ (Color figure online)
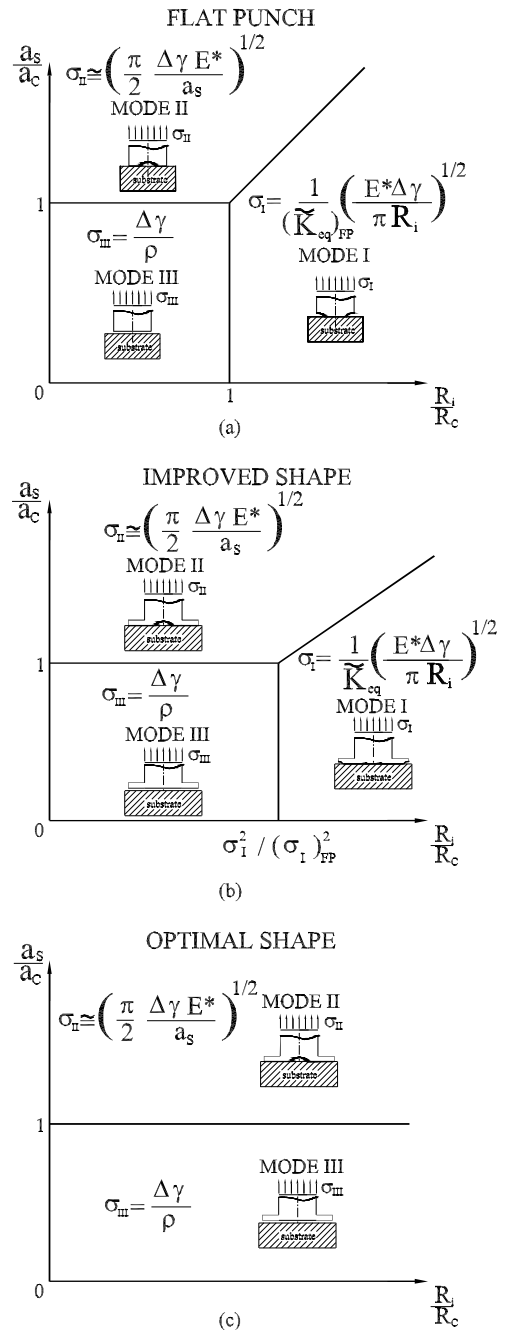

Fig. 9 The map of debonding mechanisms for a cylindrical pillar, (**a**); the modified map for a non-optimized mushroom shaped pillar, (**b**); the debonding map of an optimized mushroom shaped pillar, (**c**). The quantities $a_C = \frac{1}{2}\pi E^* \rho^2/\Delta\gamma$ and $R_C = E^*\rho^2/[\pi\Delta\gamma(\tilde{K}_{eq})^2_{FP}]$ are a reference defect size and a reference pillar radius respectively

before, $\Delta\gamma \approx 16$ mJ/m^2, $v = 0.5$, $E = 3$ MPa, and recalling that $\rho \approx 1$ nm we calculate $a_C = 0.39$ nm and $R_C = 2$ nm. For the mushroom shaped pillar [see Fig. 9(b)], the real debonding mechanism, given the defect size, depends on ratio $\sigma_I/(\sigma_I)_{FP}$. In particular, for a possible optimal pillar shape $R_e/R_i \approx 3$ and $s/R_i \approx 0.3$, we calculate $\sigma_I/(\sigma_I)_{FP} \approx 0.32 \times 10^3$, so that the mode I debonding will occur for pillars of radius $R_i \geq [\sigma_I/(\sigma_I)_{FP}]^2 \times R_C = 0.2$ mm, i.e. for optimally designed mushroom shaped micro-pillars with $R_i \approx 10$ μm and $R_e/R_i \approx 3$ mode I debonding mechanism cannot take place [see Fig. 9(c)]. Our predictions are confirmed by some experimental results [21].

Therefore we may propose a design rule of mushroom shaped micro-pillars. Indeed, on basis of our analysis the optimal pillar should be fabricated in such a way to fulfill the following geometrical constraints: $2 \leq R_e/R_i \leq 3$ and $s/R_i \approx 0.2$–0.3.

5 Interfacial entrapped air

Often during the approach of the adhesive to the substrate, air bubbles may remain entrapped at the interface. This may lead to a strong reduction of the adhesive performance, which need to be investigated. In order to carry out the analysis the total energy change of the system when a bubble of air is present at the interface must be precisely calculated. We assume that the bubble of air is much smaller than the diameter and height of the pillar so that one can treat the pillar as an elastic half-space in contact with a rigid flat surface. Assuming isothermal conditions and a constant uniform asymptotic far field tractive stress σ, the equilibrium of the system can be sought by requiring that the total free energy at the interface (i.e. the interfacial Gibbs energy) is stationary. Given the defect size and assuming a linear elastic material, the calculation of the energy change of the system must consider four different contributions (see also [46] for a different derivation): (i) the contribution to the interfacial elastic energy due to the asymptotic applied uniform tractive stress σ, (ii) the contribution to the interfacial elastic energy due the air pressure p, (iii) the internal energy of the air bubble, (iv) the variation of surface energies due to the presence of van der Waals forces. Let us consider the system shown in Fig. 10 where the bottom (initially flat) surface of an elastic half-space is glued to a rigid plate except on a circular region of
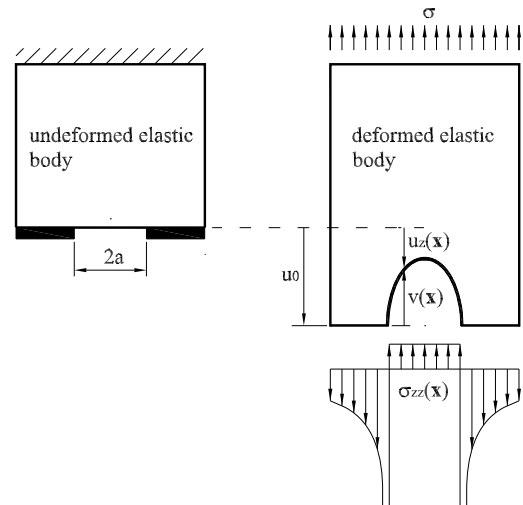

Fig. 10 The displacement, gap and stress distributions involved in the calculation of the free interfacial energy

radius a. Let us displace the rigid plate of a quantity u_0 (see Fig. 10) so that a small void is formed at the interface. Assume that the air pressure in the void is p.

To calculate the elastic energy of the system, let us first observe that the contact problem may have an equivalent formulation in terms of interfacial elastic energy, i.e. in terms of the amount of elastic energy stored at the interface as a consequence of local interfacial deformations [47]. Accordingly, the elastic interfacial energy is [47]

$$\mathcal{E} = \frac{1}{2} \int d^2x \, \sigma_{zz}(\mathbf{x}) \big[u_z(\mathbf{x}) - \langle u_z(\mathbf{x}) \rangle \big] \qquad (12)$$

where $\mathbf{x}$ is the in-plane position vector, $\sigma_{zz}(\mathbf{x})$ is the non uniform normal interfacial stress, $u_z(\mathbf{x})$ is the local normal displacement of the surface, and $\langle u(\mathbf{x}) \rangle$ is the average displacement at the interface (the symbol $\langle \cdot \rangle$ is the average operator). Considering that because of force balance the uniform stress σ at infinity is $\sigma = \langle \sigma_{zz}(\mathbf{x}) \rangle$ one can rephrase Eq. (12) as

$$\mathcal{E} = \frac{1}{2} \int d^2x \, \big[\sigma_{zz}(\mathbf{x}) - \sigma \big] u_z(\mathbf{x}) \qquad (13)$$

Now let us define (see Fig. 10) the gap distribution $v(\mathbf{x})$ as $v(\mathbf{x}) = u_0 - u_z(\mathbf{x})$. Of course $v(\mathbf{x}) \neq 0$ on the circular region of radius a, whereas it vanishes elsewhere. Using $v(\mathbf{x})$ and considering that $\sigma_{zz}(\mathbf{x}) = -p$ for $|\mathbf{x}| < a$, Eq. (13) becomes

$$\mathcal{E} = \frac{1}{2}(p + \sigma)V \qquad (14)$$

where $V = \int d^2x\, v(\mathbf{x})$ is the volume of the air bubble. The total Helmholtz free interfacial energy $\mathcal{F}$ is then the sum of the elastic interfacial energy, the free internal energy $U_A = -p_0 V_0 \ln(V/V_0)$ of the entrapped air, and the surface energy, i.e.

$$\mathcal{F}(V, a) = \mathcal{E}(V, a) + U_A(V) + \pi a^2 \Delta\gamma \quad (15)$$

From thermodynamics one concludes that under isothermal conditions and constant bubble volume V the equilibrium of the system corresponds to the stationary values of the energy $\mathcal{F}$. However, in our analysis we, instead, keep constant the asymptotic load $\langle\sigma(\mathbf{x})\rangle = \sigma$. In this case the equilibrium of the system corresponds to the stationary values of the interfacial Gibbs energy $\mathcal{G}(\sigma, a)$. Following the standard approach of thermodynamics [48], we obtain $\mathcal{G}(\sigma, a)$ by enforcing a Legendre transformation, i.e.

$$\mathcal{G}(\sigma, a) = \mathcal{F}(V, a) - \left.\frac{\partial \mathcal{F}}{\partial V}\right|_a V \quad (16)$$

Observing that $\partial\mathcal{E}/\partial V|_a = p + \sigma$ and $\partial U_A/\partial V|_a = -p$, one yields the required expression for the interfacial Gibbs energy $\mathcal{G}$, i.e.

$$\mathcal{G}(\sigma, a) = \Delta U_{tot} = \frac{1}{2}(p - \sigma)V + U_A + \pi a^2 \Delta\gamma \quad (17)$$

Beside Eq. (17) two additional equations are needed

$$pV = p_0 V_0 \quad (18)$$

and

$$V = \frac{8a^3}{3E^*}(\sigma + p) \quad (19)$$

Equations (18), (19) allow to calculate the quantity V and p as a function of the radius a of the non contact circular area. Therefore, the total energy change ΔU_{tot} given by Eq. (17) finally depends only on the applied constant stress σ and the size of the voids a. By following a similar approach as in JKR theory [49], requiring that $\partial \Delta U_{tot}/\partial a|_\sigma = 0$ allows to calculate the values of a at equilibrium, given the applied uniform stress σ. The critical pull-off stress σ_{cr}, which destabilize the defect and causes the detachment of the pillar from the rigid flat substrate, is determined by requiring that at equilibrium the relation $\partial^2 \Delta U_{tot}/\partial a^2|_\sigma = 0$ is also satisfied.

The above equations can be rephrased in a dimensionless form. To this end let us define the adhesion length $\delta = \Delta\gamma/E^*$ and the dimensionless quantities
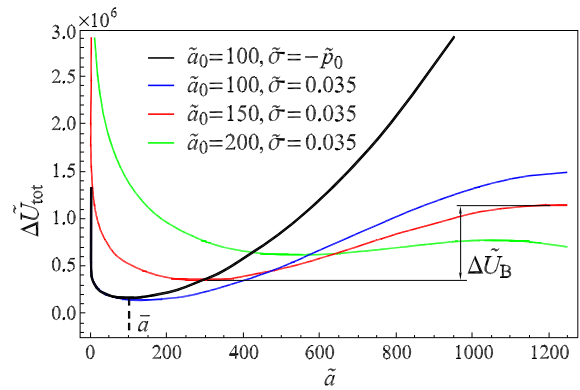

Fig. 11 The dimensionless total energy $\Delta\tilde{U}_{tot}$ as a function of the radius of the detached area $\tilde{a}$, for three different values of the initial radius $\tilde{a}_0$, given the same value of dimensionless stress $\tilde{\sigma} = 0.035$ (*blue*, *red* and *green curves*). Increasing $\tilde{a}_0$ determines a decrease of the energy barrier $\Delta\tilde{U}_B$ between the stable and unstable equilibrium states. The *solid black curve* represents the total energy as a function of $\tilde{a}$ when the pillar is subjected to the environment pressure only, i.e. $\tilde{\sigma} = -\tilde{p}_0$, and for $\tilde{a}_0 = 100$. Notice that in this case there is only one equilibrium condition at $\tilde{a} = \bar{a}$ which is necessarily stable (Color figure online)

$\tilde{\sigma} = \sigma/E^*$, $\tilde{p} = p/E^*$, $\tilde{a} = a/\delta$, $\tilde{V} = V/\delta^3$. The dimensionless total energy change of the system is therefore $\Delta\tilde{U}_{tot} = \Delta U_{tot}/(\delta^3 E^*)$, where $\tilde{V} = (8/3)(\tilde{\sigma} + \tilde{p})\tilde{a}^3$ and $\tilde{p}\tilde{V} = \tilde{p}_0\tilde{V}_0$.

We assume that the environment pressure is 1 bar, so that the initial pressure of the entrapped air bubble is also $p_0 = 0.1$ MPa. We also notice that the asymptotic applied stress σ is $\sigma = \sigma_0 - p_0$, where $\sigma_0 = P/A$ is the external applied average stress, P the applied load and A the cross section area of the pillar. Figure 11 shows the total dimensionless energy change $\Delta\tilde{U}_{tot}$ as a function of the dimensionless radius $\tilde{a}$, for different values of the initial dimensionless size $\tilde{a}_0$ of the void. In our calculations we have used $\sigma = 0.2$ MPa (i.e. $\sigma_0 = 0.3$ MPa), $\Delta\gamma \approx 16$ mJ/m^2, $E = 3$ MPa and $\nu = 0.5$. The figure shows that for any value of $\tilde{a}_0$, two equilibrium conditions exist, i.e. the stable state (energy minimum) and the unstable state (energy maximum). However, as expected, when the asymptotic applied stress is zero or even negative only a stable equilibrium state must be present (see the black line in Fig. 11 with $\tilde{a}_0 = 100$ and $\tilde{\sigma} = -\tilde{p}_0$, i.e. $\tilde{\sigma}_0 = 0$). When an external stress $\sigma > 0$ is applied, an energy barrier must be exceeded in order to destabilize the system. The energy barrier $\Delta\tilde{U}_B$ in this case is defined as the difference between the energy value of the unstable equilibrium state and the energy value of the sta-
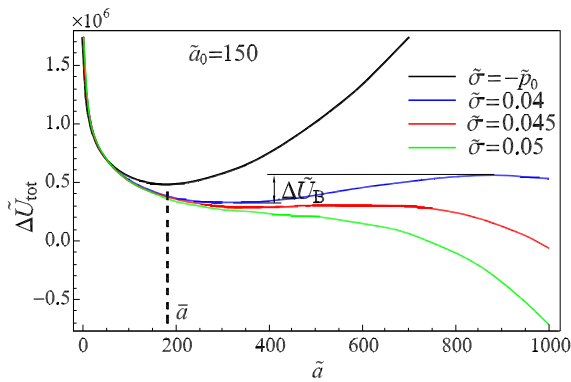
Fig. 12 The dimensionless total energy $\Delta \tilde{U}_{tot}$ as a function of the radius of the detached area $\tilde{a}$, for four different values of the applied stress $\tilde{\sigma}$, and for $\tilde{a}_0 = 150$. Increasing $\tilde{\sigma}$ determines a decrease of the energy barrier $\Delta \tilde{U}_B$ between the stable and unstable equilibrium states until it vanishes and the air bubble is destabilized (Color figure online)
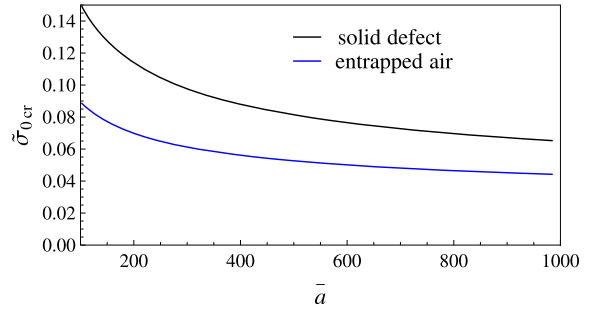

Fig. 13 The dimensionless external critical stress $\tilde{\sigma}_{0cr} = \tilde{\sigma}_0 + \tilde{p}_0$ as a function of the air bubble or solid particle size $\bar{a}$ (see text for more details). The *blue curve* refer to the air bubble case, the *black curve* to the interfacial solid particle case (Color figure online)

ble equilibrium state. From Fig. 11, given the same applied stress, one observes that the energy barrier $\Delta \tilde{U}_B$ decreases as the initial radius $\tilde{a}_0$ of the bubble (i.e. its initial volume) is increased. When $\Delta \tilde{U}_B = 0$, i.e. when $\partial \Delta U_{tot}/\partial a|_\sigma = 0$ and $\partial^2 \Delta U_{tot}/\partial a^2|_\sigma = 0$, the critical defect size $(\tilde{a}_0)_{cr}$ is found which prevents the pillar from adhering to the substrate.

Given the initial defect size $\tilde{a}_0$, one may also analyze what happens when the applied stress σ is increased. In particular, Fig. 12 shows that, for a fixed value of the radius $\tilde{a}_0$ (we have considered $a_0 = 0.6 \, \mu m$, i.e. $\tilde{a}_0 = 150$), when the applied stress σ increases an unstable equilibrium state appears, which is again separated from the corresponding stable equilibrium by an energy barrier $\Delta \tilde{U}_B$. As the stress $\tilde{\sigma}$ is further increased, the energy barrier $\Delta \tilde{U}_B$ decreases and vanishes at a certain stress level $\tilde{\sigma}_{cr}$ (the so called critical pull-off stress) at which the air bubble of initial size $\tilde{a}_0$ is destabilized and the pillar detaches from the substrate.

It is interesting now to compare the critical stress in case of solid defects of size a_S (dust particles, impurities, etc.) $\sigma_{II} = [\pi \Delta \gamma E^*/(2a_S)]^{1/2}$ with the critical pull-off stress σ_{cr} obtained in the case a bubble of air entrapped at the interface. The comparison must be carried out assuming that, at $\tilde{\sigma} = -\tilde{p}_0$ (i.e. $\tilde{\sigma}_0 = 0$), the (dimensionless) size $\bar{a}$ of the air bubble at equilibrium is identical to the (dimensionless) solid defect size, i.e. $\bar{a} = \tilde{a}_S$. Figure 13 compares the critical stress $\tilde{\sigma}_{0cr} = \tilde{\sigma}_{cr} + \tilde{p}_0$ in the two cases as a function of the radius $\bar{a}$. We observe that, in the case of

air bubble, the debonding stress $\tilde{\sigma}_{0cr}$ is always significantly smaller than the one obtained in the case of solid defects with a reduction of about 35–40 % over the entire range of defect size considered in the calculation, i.e. $\bar{a} = \tilde{a}_S = 0.4$–4 μm. Indeed, micro-air bubbles weaken the adhesive link between the pillar and the rigid substrate more than the presence of external particles, since their gas pressure exerts an additional debonding force and reduce the suction effect which contributes to keep the pillar in contact with the substrate. This represents a practical problem during fast attaching-detaching of this kind of microstructure, since in this case the entrapment of air can hardly be avoided.

6 The influence of non uniform pillar height distribution

Cylindrical or mushroom-shaped micropillars have been employed to fabricate microstructured highly-adhesive glue-free surfaces. However, during the fabrication process it is very complicated to exactly control the height of each single pillar, i.e. some pillars will be taller and other smaller than the nominal height (see Fig. 14).

Here we analyse the effect of non uniform pillar height distribution. Referring to Fig. 14 we assume that the nominal pillar height is l, then the height h of the pillar can be written as $h = l + z$, where we assume that the distances z are distributed according to a Gaussian probability density distribution

$$p(z) = \frac{1}{\sqrt{2\pi \langle z^2 \rangle}} \exp\left(-\frac{z^2}{2\langle z^2 \rangle}\right) \qquad (20)$$
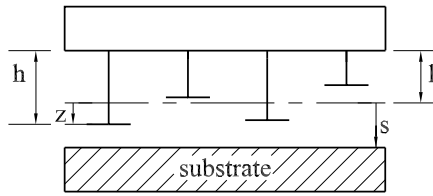
Fig. 14 A microstructured surface covered with mushroom-shaped pillars. Some pillars are taller and others smaller than the nominal height. The nominal pillar height is l, the actual height h of the pillar can be written as $h = l + z$
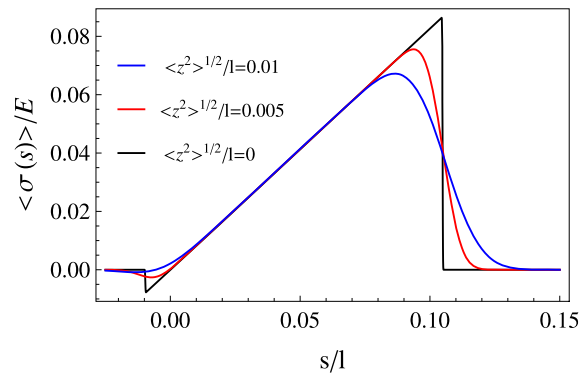

Fig. 15 The mean stress $\langle \sigma(s) \rangle$ in units of the elastic modulus E of the material, as a function of the dimensionless separation s/l for different values of the quantity reduced root mean square (rms) distance $\langle z^2 \rangle^{1/2}/l$ (Color figure online)

where $\langle \ \rangle$ is the statistical average operator, and $\langle z^2 \rangle$ is the mean square distance. Now assume that, after preloading, all pillars come into contact with the substrate. Therefore, assuming that the substrate is located at a distance s from the mean plane $z = 0$, we can calculate the force needed to elongate the fibre as

$$F = \pi R^2 E \frac{s - z}{l + z} \tag{21}$$

where R is the circular radius of the pillar cross section. Observe that the force F increases with $s - z$ up to the limiting pull-off value $F_{out} = \pi R_\sigma^2 \sigma_{II}$ at which the pillar will detach from the substrate. Also observe that if the quantity $s - z$ is less than zero then a compressive (negative) force will act on the pillar, and this compressive force will increase as $s - z$ is decreased down to a limiting (negative) load F_B, which causes the elastic buckling of the pillar

$$F_B = -\pi^2 E J / \left[2(l + z) \right]^2 \tag{22}$$

where $J = \pi R^4 / 4$. We assume that below this value the pillar is not able to support the load. Thus, we can calculate, as a function of s, the range of distances z, that will contribute to the total force acting on the microstructured surface. By requiring that $F_B < F < F_{out}$, one obtains $z_{\min}(s) < z < z_{\max}(s)$ where

$$z_{\min}(s) = l \left(\frac{s}{l} - \frac{R_\sigma^2}{R^2} \frac{\sigma_{II}}{E} \right) \left(1 + \frac{R_\sigma^2}{R^2} \frac{\sigma_{II}}{E} \right)^{-1} \tag{23}$$

$$z_{\max}(s) = \frac{l}{2} \left[\sqrt{ \left(1 + \frac{s}{l} \right)^2 + \pi \frac{J}{l^2 R^2} } - \left(1 - \frac{s}{l} \right) \right] \tag{24}$$

and the average stress $\langle \sigma(s) \rangle$ in units of E at equilibrium is

$$\frac{\langle \sigma(s) \rangle}{E} = \int_{z_{\min}(s)}^{z_{\max}(s)} p(z) \frac{s - z}{l + z} \, dz \tag{25}$$

Let us consider, as before, the case of a microstructured surface made of PVS ($\Delta \gamma \approx 16$ mJ/m^2, $E^* = 4$ MPa) covered with mushroom-shaped pillars with internal radius $R = 12.5$ μm and nominal pillar height $l = 100$ μm [33]. Assuming a limiting pull-off stress $\sigma_{II} \approx 0.26$ MPa (see Sect. 3), we obtain the average stress $\langle \sigma(s) \rangle$ in units of E as a function of the dimensionless separation s/l for different values of the reduced root mean square (rms) distance $\langle z^2 \rangle^{1/2}/l$ as shown in Fig. 15.

Figure 15 shows the strong reduction of the average stress $\langle \sigma(s) \rangle$, which occurs as the quantity $\langle z^2 \rangle^{1/2}/l$ is increased. In particular the maximum dimensionless pull-off stress $\langle \sigma \rangle_{\max}/E$ can be plot as a function of $\langle z^2 \rangle^{1/2}/l$. Figure 16 shows, indeed, that a value of the rms distance $\langle z^2 \rangle^{1/2}$ equal to ≈ 1 % of the nominal height l is already enough to produce a decrement of the pull-off stress of about ≈ 20 %.

7 Stress aided thermally activated defect nucleation

The above calculations have been carried out for cases where defects are already present at the interface between the micro-pillars and the substrate. However, in some conditions the surfaces may be very clean and very smooth. When this happens one may be tempted to conclude that, not depending on the type of pillar we are considering, mode II debonding mechanism can never occur. In particular one would expect that cylindrical pillars would detach by following mode I
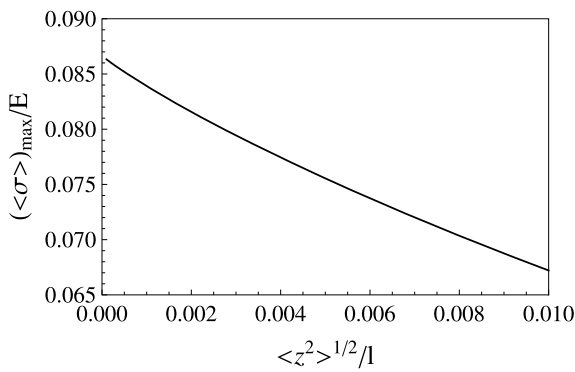
Fig. 16 The maximum average stress $\langle\sigma\rangle_{max}$ (in units of the elastic modulus E) as a function of $\langle z^2\rangle^{1/2}/l$

Fig. 17 Map of debonding mechanisms for a cylindrical micropillar in contact with perfectly clean and smooth substrates

or mode III mechanisms, whereas mushroom-shaped pillars would detach by following mode III only. However, in this section we show that this is not true and that mode II remains a possible debonding mechanism since defects at the interface may be formed as a consequence of a stress aided thermally activated nucleation process. Indeed, thermal fluctuations are always able to overcome the stress dependent energy barrier $\Delta U_B = \pi^3 \Delta\gamma^3 E^{*2}/(12\sigma^4)$ (see [30]) and nucleate the defect. Statistical mechanics shows that the rate w at which these fluctuations occur depends on the energy barrier ΔU_B through the Maxwell-Boltzmann equation $w = \nu \exp(-\Delta U_B/k_B T)$, where T is the temperature of the system, $\nu \approx 10^{14}$ s^{-1} is a very large prefactor related to the high entropy associated with placing the nucleus in many different places on the contact area [10] and k_B is the Boltzmann constant. We observe that, increasing the applied stress determines a strong reduction of the energy barrier ΔU_B and therefore an increase of the nucleation rate. Of course, if the applied stress is small one must wait a long time before the first nucleus is formed and pillar detachment can be observed. However, as the applied stress is increased, defect nucleation and pillar detachment will occur on shorter time intervals and will become observable when these time intervals will reach values of order 1 s or less, i.e. when the nucleation rate w is equal to or smaller than $w_0 \approx 1$ Hz. When this happens the stress-dependent energy barrier takes the value $\Delta U_B = k_B T \ln(\nu/w_0)$. At room temperature, i.e. $T = 300$ K, one obtains $\Delta U_B \approx 1$ eV.

This means that mode II debonding mechanism can be observed, even in case of perfectly smooth and clean surfaces, when the applied stress is large enough
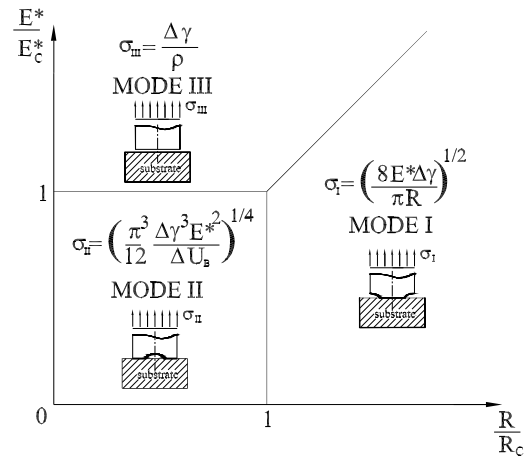
to reduce the energy barrier against nucleation at values equal to or smaller than $\Delta U_B \approx 1$ eV. From ΔU_B one can calculate the critical external stress σ_{II} which activates the stress aided thermally activated debonding mechanism of type II:

$$\sigma_{II} = \left[\frac{\pi^3}{12} \frac{\Delta\gamma^3 E^{*2}}{\Delta U_B} \right]^{1/4} \quad (26)$$

For the case of PVS micropillars under consideration one obtains $\sigma_{II} = 5$ MPa. This value is relatively large and may be even larger than the rupture stress of the fibre. This of course means that soft micropillars might be, in principle, ripped off before mode II debonding can take place. Now, neglecting other forms of failure, and concentrating only on interfacial detachment, one can produce a new map of debonding mechanisms for the case of cylindrical micropillars in contact with clean and smooth surfaces.

This new map is shown in Fig. 17, where

$$E_C^* = \left(\frac{12}{\pi^3} \frac{\Delta\gamma \Delta U_B}{\rho^4} \right)^{1/2} \quad (27)$$

Recalling that $\Delta U_B \approx 1$ eV, and that for PVS micropillars $\Delta\gamma \approx 0.016$ J/m^2 and $\rho \approx 1$ nm one obtains that the stress-aided thermally activated nucleation at the interface is energetically more favorable than uniform decohesion (mode III) when $E^* < E_C^* = 31$ MPa. Hence, in case of PVS ($E^* = 4$ MPa) cylindrical micro-pillars we expect that only mode I and mode II debonding mechanisms can be activated. To find which one is the real mechanism it is enough to
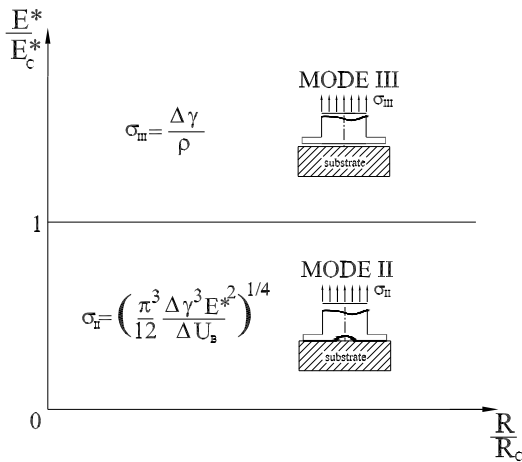
Fig. 18 Map of debonding mechanisms for an optimally designed mushroom shaped micropillar in contact with a perfectly clean and smooth substrate

observe that mode I mechanism occurs when $\sigma_I < \sigma_{II}$, which gives

$$R > R_C = \sqrt{\frac{768}{\pi^5}\frac{\Delta U_B}{\Delta\gamma}} \tag{28}$$

Being $\Delta\gamma \approx 0.016$ J/m^2, we obtain $R_C \approx 5$ nm which simply means that, even in case of contact with perfectly smooth and clean surfaces, man-made cylindrical PVS micropillars (size of order 10 μm [33]) always detach from the substrate by following the mode I debonding mechanism.

However the presence of an optimally designed annular plate inhibits mode I failure mechanism, thus, in the case of mushroom-shaped pillar in contact with perfectly smooth and clean surface, the map of debonding mechanisms changes as shown in Fig. 18, from which one concludes that relatively soft mushroom-shaped pillars detach at much higher stress because of stress aided thermally activated defect nucleation (mode II mechanism) even in case of clean and smooth surfaces.

8 Conclusions and outlook

We have reviewed the main detachment mechanisms of microstructured adhesives made of regular arrays of micropillars and shown how mushroom shaped micropillars can be optimally designed to strongly enhance the performance of this type of biomimetic adhesives. Although these optimized systems present pull-off forces which may be even larger than those obtained in the case of biological systems (e.g. geckos and beetles), they present direction-independent adhesion, i.e. the strength of adhesion is the same not depending on the direction of the applied load. This is an important drawback when the goal is related to applications in the field of locomotion and object manipulation. We may say that, notwithstanding the great advances in the field of microstructured adhesives, our attempt to copy Nature is incomplete. Indeed, a lot of research is still going on and will be needed in the future to propose and fabricate bio-mimetic surfaces with controlled direction dependent adhesion.

References

1. http://en.wikipedia.org/wiki/Bionics
2. Geim AK et al (2003) Nat Mater 2(7):461
3. Kim T, Jeong HE, Suh KY, Lee HH (2009) Adv Mater 21:2276–2281
4. Lee H, Lee BP, Messersmith PB (2007) Nature 448:338–342
5. Majidi C, Groff RE, Maeno Y, Schubert B, Baek S, Bush B, Maboudian R, Gravish N, Wilkinson M, Autumn K, Fearing RS (2006) Phys Rev Lett 97:076103
6. Spolenak R, Gorb S, Artz E (2005) Acta Biomater 1:5–13
7. del Campo A, Greiner C, Arzt E (2007) Langmuir 23:10235–10243
8. Greiner C, Spolenak R, Arzt E (2009) Acta Biomater 5:597–606
9. Greiner C, del Campo A, Arzt E (2007) Langmuir 23:3495–3502
10. Persson BNJ, Volokitin AI, Tosatti E (2003) Eur Phys J E 11:409–413
11. Persson BNJ (2003) Wear 254:832–834
12. Persson BN, Gorb S (2003) J Chem Phys 119:11437–11444
13. Carbone G, Persson BNJ (2004) J Chem Phys 121:2246–2252
14. Autumn K, Liang YA, Hsleh ST, Zesch W, Chan WP, Kenny TW, Fearilng R, Full RJ (2000) Nature 405:681–686
15. Carbone G, Mangialardi L, Persson BNJ (2004) Phys Rev B 70:125407
16. Carbone G, Decuzzi P (2004) J Appl Phys 95:4476–4482
17. Persson BNJ, Albohr O, Tartaglino U, Volokitin AI, Tosatti E (2005) J Phys Condens Matter 17:R1–R62
18. Scherge M, Gorb S (2001) Biological micro- and nanotribology. Springer, Berlin
19. Kim S, Sitti M (2006) Appl Phys Lett 89:261911
20. Varenberg M, Pugno NM, Gorb S (2010) Soft Matter 6:3269–3272
21. Varenberg M, Gorb S (2008) J R Soc Interface 5:785–789
22. Kwak MK, Jeong H-E, Bae W-G, Jung H-S, Suh KY (2011) Small 7:2296–2300
23. Noderer WL, Shen L, Vajpayee S, Glassmaker NJ, Jagota A, Hui C-Y (2007) Proc R Soc A 463:2631–2654

24. Glassmaker NJ, Jagota A, Hui C-Y, Noderer WL, Chaudhury MK (2007) Proc Natl Acad Sci USA 104:10786–10791
25. Afferrante L, Carbone G (2012) J R Soc Interface. doi:10.1098/rsif.2012.0452
26. Murphy MP, Kim S, Sitti M (2009) Appl Mater Interfaces 1(4):849–855
27. Daltorio KA, Gorb S, Peressadko A, Horchler AD, Ritzmann RE, Quinn RD (2005) In: Proc int conf climbing and walking robots, pp 131–138
28. Gorb SN, Varenberg M (2007) J Adhes Sci Technol 21:1175–1183
29. Varenberg M, Gorb S (2007) J R Soc Interface 4:721–725
30. Carbone G, Pierro E, Gorb S (2011) Soft Matter 7:5545–5552
31. Karp JM, Langer R (2011) Nature 477:42–43
32. Kwak MK, Jeong H-E, Suh KY (2011) Adv Mater. doi:10.1002/adma.201101694
33. Gorb S, Varenberg M, Peressadko A, Tuma J (2007) J R Soc Interface 4:271–275
34. Bogy DB (1971) Two edge-bonded elastic wedges of different materials and wedge angles under surface tractions. J Appl Mech 38(2):377
35. Buckingham E (1914) Phys Rev 4:345–376
36. Buckingham E (1915) Nature 96:396–397
37. Tang T, Hui C-Y, Glassmaker NJ (2005) Can a fibrillar interface be stronger and tougher than a non-fibrillar one? J R Soc Interface 2(5):505–516
38. Spuskanyuk AV, McMeeking RM, Deshpande VS, Arzt E (2008) Acta Biomater 4:1669–1676
39. Gorb S. Private communication
40. Timoshenko SP, Woinowsky-Kreiger S (1959) Theory of plates and shells, 2nd edn. Engineering mechanics series. McGraw-Hill, London. ISBN 0-07-085820-9
41. Landau LD, Lifshitz EM (1959) Theory of elasticity. Pergamon, London
42. Glassmaker NJ, Jagota A, Hui CY, Noderer WL, Chaudhury MK (2007) Proc Natl Acad Sci USA, 104(26):10786–10791
43. Maugis D (1999) Contact, adhesion and rupture of elastic solids. Springer Series in Solid State Sciences. Springer, Berlin, Heidelberg, New York
44. Carbone G, Pierro E (2012) Small 8(9):1449–1454
45. ANSYS, User's manual. Version 10.0
46. Carbone G, Pierro E (2012) Soft Matter 8:7904–7908
47. Carbone G, Mangialardi L (2008) J Mech Phys Solids 56(2):684–706
48. Callen HB (1985) Thermodynamics and an introduction to thermostatistics. Wiley, USA ISBN 0-471-86256-8
49. Johnson KL, Kendall K, Roberts AD (1971) Proc R Soc Lond A 324:301–313